AGU PUBLICATIONS

JGR

Journal of Geophysical Research: Space Physics

RESEARCH ARTICLE

10.1002/2015JA022048

Special Section:
Inner Magnetosphere
Coupling: Recent Advances

Key Points:
- Magnetosphere responds as a resonant waveguide to ULF fluctuations in solar wind dynamic pressure
- Inclusion of a plasmasphere has a substantial impact on the nature of the simulated ULF waves
- Inclusion of a plasmasphere leads to a deeper penetration of azimuthal electric field oscillations

Supporting Information:
- Figures S1–S4 and Caption for Movie S1
- Movie S1

Correspondence to:
S. G. Claudepierre,
sethclaudepierre@gmail.com

Citation:
Claudepierre, S. G., F. R. Toffoletto, and M. Wiltberger (2016), Global MHD modeling of resonant ULF waves: Simulations with and without a plasmasphere, *J. Geophys. Res. Space Physics*, *121*, 227–244, doi:10.1002/2015JA022048.

Received 17 OCT 2015
Accepted 7 DEC 2015
Accepted article online 13 DEC 2015
Published online 13 JAN 2016

Global MHD modeling of resonant ULF waves: Simulations with and without a plasmasphere

S. G. Claudepierre[1], F. R. Toffoletto[2], and M. Wiltberger[3]

[1]Space Sciences Department, Aerospace Corporation, El Segundo, California, USA, [2]Physics and Astronomy Department, Rice University, Houston, Texas, USA, [3]High Altitude Observatory, National Center for Atmospheric Research, Boulder, Colorado, USA

Abstract We investigate the plasmaspheric influence on the resonant mode coupling of magnetospheric ultralow frequency (ULF) waves using the Lyon-Fedder-Mobarry (LFM) global magnetohydrodynamic (MHD) model. We present results from two different versions of the model, both driven by the same solar wind conditions: one version that contains a plasmasphere (the LFM coupled to the Rice Convection Model, where the Gallagher plasmasphere model is also included) and another that does not (the stand-alone LFM). We find that the inclusion of a cold, dense plasmasphere has a significant impact on the nature of the simulated ULF waves. For example, the inclusion of a plasmasphere leads to a deeper (more earthward) penetration of the compressional (azimuthal) electric field fluctuations, due to a shift in the location of the wave turning points. Consequently, the locations where the compressional electric field oscillations resonantly couple their energy into local toroidal mode field line resonances also shift earthward. We also find, in both simulations, that higher-frequency compressional (azimuthal) electric field oscillations penetrate deeper than lower frequency oscillations. In addition, the compressional wave mode structure in the simulations is consistent with a radial standing wave oscillation pattern, characteristic of a resonant waveguide. The incorporation of a plasmasphere into the LFM global MHD model represents an advance in the state of the art in regard to ULF wave modeling with such simulations. We offer a brief discussion of the implications for radiation belt modeling techniques that use the electric and magnetic field outputs from global MHD simulations to drive particle dynamics.

1. Introduction

1.1. Magnetospheric ULF Pulsations

Resonant ultralow frequency (ULF) mode coupling theory provides a theoretical framework for the quasi-monochromatic fluctuations ($T\sim$ minutes) frequently observed in both ground-based magnetometer and spacecraft magnetic and electric field measurements [e.g., *Chen and Hasegawa*, 1974a]. In this theory, a monochromatic fast compressional mode wave is assumed to originate in the outer magnetosphere (e.g., at the magnetopause). As the monochromatic fast mode wave propagates earthward, it encounters regions of increasing Alfvén speed, until the wave frequency matches the local field line eigenfrequency. Here the classical turning point is reached, beyond which the compressional mode becomes evanescent and couples its energy into the transverse, shear Alfvén mode. This is the field line resonance (FLR) mechanism. This theory has been successful in explaining many features of ground-based and in situ ULF observations [*Hughes*, 1994, and references therein].

The MHD wave equations that describe ULF pulsations are coupled and cannot be solved analytically in realistic magnetospheric geometries. However, two limiting cases on the azimuthal wave number, m, can be used to simplify and decouple the equations in a dipole field geometry. In the limit of large and small m values, the equations fully decouple and describe three oscillation modes: the poloidal Alfvén mode ($m\rightarrow\infty$), the toroidal Alfvén mode ($m\rightarrow 0$), and the fast compressional mode ($m\rightarrow 0$). In the poloidal mode, each dipole magnetic field line oscillates in the radial direction, with the oscillation confined to a fixed meridional plane. Thus, the oscillations are in the v_r, B_r, and E_φ field components, where r and φ are the radial and azimuthal directions, respectively. By contrast, in the toroidal mode of oscillation, the perturbations are in the v_φ, B_φ, and E_r field components and entire L shells oscillate azimuthally. In the $m\rightarrow 0$ decoupling limit, there is an additional mode of oscillation, known as the fast compressional mode. Here the perturbations are in the v_r, B_r, $B_\parallel$, and E_φ field components, where $\parallel$ represents the direction along the background magnetic field.

The full decoupling into these three modes is a mathematical convenience. In reality, magnetospheric ULF waves have a finite wave number and show a mixture of more than one and, at times, all three polarizations. Wave observations are typically reported in terms of the dominant polarization.

1.2. The Role of ULF Pulsations in Radiation Belt Dynamics

There are two nonadiabatic transport processes that are believed to govern the large-scale electron dynamics in the Earth's radiation belts: local acceleration and radial transport. Local acceleration results from resonant wave-particle interactions; magnetospheric chorus waves are believed to play a dominant role. These waves have frequencies on the order of the electron gyrofrequency at typical radiation belt energies (~100–1000 keV) and can therefore violate the first adiabatic invariant of the charged particle motion. On the other hand, radial transport involves a violation of the third adiabatic invariant while simultaneously conserving the first and second invariants. Such transport is mediated by field fluctuations in the millihertz frequency range and can be separated into two categories: prompt acceleration and radial diffusion. In both cases, a drift-resonant interaction occurs where an individual particle experiences a constant wave electric field over its azimuthal drift orbit. This resonant interaction is governed by the equation $\omega = m\omega_d$, where ω is the ULF wave frequency, m is the azimuthal mode number of the interacting wave, and ω_d is the electron drift frequency [*Hudson et al.*, 2000].

Radiation belt electrons can experience a nondiffusive, prompt acceleration via coherent drift-resonant interactions. These rapid accelerations are typically mediated by intense, shock-induced compressional waves (e.g., the extreme case of the 24 March 1991 event [*Li et al.*, 1993]) but have also been observed under more modest driving conditions [*Tan et al.*, 2011]. Radial diffusion, on the other hand, is produced by incoherent scattering in the third invariant. Here drift-resonant interactions occur between electrons and magnetospheric ULF waves in the Pc4–5 band ($f \approx 1-20$ mHz) and the diffusion rate is directly proportional to wave power in this frequency range. Evidence for this relationship is found in the observed correlation between solar wind speed increases and radiation belt electron flux enhancements [e.g., *Paulikas and Blake*, 1979]. Pc4–5 ULF waves have been proposed as the intermediary physical mechanism responsible for this observed correlation, as solar wind speed is strongly correlated with ULF wave power [e.g., *Mathie and Mann*, 2001] and a number of studies have reported a clear relationship between variations in electron flux and ULF wave power [*Rostoker et al.*, 1998; *Baker et al.*, 1998; *Mathie and Mann*, 2000; *Green and Kivelson*, 2001]. This suggests that magnetospheric ULF waves may, at times, play a role in the acceleration of radiation belt electrons to MeV energies. These solar-wind-driven, low-m number ($m < 20$), and low-frequency (0–30 mHz/Pc3-5) ULF waves will be the focus of this investigation.

There is increasing evidence that both local acceleration and radial transport contribute to electron energization in the outer zone [e.g., *Thorne*, 2010]. For example, recent observational [*Reeves et al.*, 2013] and theoretical works [*Thorne et al.*, 2013] have suggested that the local acceleration of hundreds of keV electrons, via interaction with magnetospheric chorus waves, is responsible for the prompt, rapid acceleration of electrons to multi-MeV energies observed in the heart of the outer zone (e.g., $L \approx 4$). On the other hand, radial transport driven primarily by magnetospheric ULF waves likely plays a role in longer-timescale energization events, where the outer zone MeV fluxes build up slowly over several days [*Ozeke et al.*, 2014]. In addition, outward radial diffusion driven by ULF waves is also believed to be important in global-scale electron dropout events during storm main phase, where outer zone electrons encounter a compressed magnetopause along their azimuthal drift, a process known as "magnetopause shadowing" [*Shprits et al.*, 2006; *Hudson et al.*, 2014]. Rapid electron acceleration to MeV energies via coherent ULF wave interactions has also been reported [e.g., *Zong et al.*, 2009]. It is likely that these mechanisms all act in concert and contribute to the overall state and configuration of the outer radiation belt. The degree to which each process (along with others not described here) contributes in a given event is an area of active and intense research. Thus, accurate modeling of both local acceleration and radial transport, along with a variety of loss mechanisms, is crucial toward understanding outer zone electron dynamics to the point of predictability.

1.3. Radiation Belt and ULF Wave Modeling

We can describe, test, and expand our understanding of electron dynamics in the Earth's radiation belt through modeling, of which there are numerous approaches: magnetohydrodynamic (MHD) test particle, data assimilation, and numerically solving the Vlasov equation in the quasi-linear regime. Some of these approaches require the specification of one or more diffusion coefficients. For example, in the quasi-linear approach, the Fokker-Planck equation is solved with appropriate boundary conditions, resulting in diffusion in momentum, pitch angle and L shell. The diffusion rates are governed by a 3×3 tensor where the diagonal terms correspond to the diffusion coefficients along one dimension [*Schulz and Lanzerotti*, 1974]. To model a given relativistic electron acceleration event, these diffusion coefficients must be specified and are typically obtained from statistical wave power maps (observational averages over mission-long timescales). Thus, such diffusion coefficients are accurate only in the statistical sense, and their use in event studies—the ultimate predictive goal—is questionable.

In the MHD test particle approach [e.g., *Kress et al.*, 2007], a global MHD simulation is performed for a given event, driven by solar wind parameters measured at an upstream monitor. Test particle trajectories are then traced in the time-dependent output fields from the magnetospheric simulation. The rates of energization, transport, and loss of the test particles are thus governed primarily by the interaction of the particles with the fluctuating electric and magnetic fields (the large-scale magnetospheric configuration also plays a role, particularly in particle loss). Thus, in this approach, the radial diffusion coefficient is defined implicitly through the ULF fluctuations in the simulated electric and magnetic fields. This has the distinct advantage that the rates of radial transport for a given event are determined directly from the simulated electric and magnetic fields. Thus, accurate radial transport can be reproduced for a given event, so long as the global MHD model is able to realistically simulate the ULF wave fields. In particular, if the spatial distribution (radial and azimuthal extent), spectral characteristics (wavelength and frequency), polarization, and intensity of the ULF waves are not reproduced in a physically consistent manner for a given event, the particle transport results are inaccurate and may not be representative of the true state of the radiation belt.

In the present study, we use the Lyon-Fedder-Mobarry (LFM) model, coupled to the Rice Convection Model (RCM), to simulate magnetospheric ULF waves driven by solar wind dynamic pressure fluctuations, with a particular focus on the role that the plasmasphere plays in the modeling of such waves. The LFM-RCM numerical model is considerably more sophisticated than those that have been used in the past to simulate resonant ULF waves in the magnetosphere. Previous efforts have been limited by various assumptions and simplifications regarding model geometry, boundary conditions, and ULF wave generation mechanisms. For example, numerical models such as *Allan et al.* [1986a] and *Lee and Lysak* [1989] consider resonant ULF mode coupling in closed geometries, where the primary source of energy dissipation is into the ionosphere (the other being numerical dissipation). In contrast, the LFM-RCM realistically models the entire magnetospheric cavity, and solar wind-driven energy that enters the magnetosphere on the dayside can be lost naturally into the magnetotail. Moreover, in the earlier models, the azimuthal mode number spectrum of the resonant ULF waves is imposed on the simulation, whereas this spectrum falls naturally out of the LFM-RCM simulation. We emphasize this point, as knowledge of the azimuthal mode number spectrum is crucial for quantifying the role that ULF waves play radiation belt dynamics. Furthermore, while the earlier numerical ULF models account for the various boundary conditions that are important for resonant ULF mode coupling (e.g., ionosphere, plasmasphere, and magnetopause), they do not employ realistic physical models of these regions, as is done in the LFM-RCM. More recent modeling efforts have improved on some of these deficiencies [*Rickard and Wright*, 1994; *Lee and Lysak*, 1999; *Waters et al.*, 2000; *Proehl et al.*, 2002; *Waters and Sciffer*, 2008; *Degeling et al.*, 2010], though no numerical model to date has demonstrated resonant ULF mode coupling in a 3-D, global-scale simulation of the magnetosphere-ionosphere-solar-wind interaction that includes a plasmasphere. As is demonstrated below, the new, coupled LFM-RCM specifically includes significant mass density and adiabatic plasmas that are absent from the stand-alone LFM. The inclusion of these plasmas substantially influences the simulated ULF wave fields. Thus, the current investigation is an advance over previous work, in that we are able to consider resonant mode coupling in a more realistic representation of the Earth's magnetosphere.

The overarching goal of the present work is to compare simulated ULF waves in two models driven by the same solar wind conditions: one model with a plasmasphere and one without a plasmasphere. The remainder of the paper is organized as follows. In section 2, we describe the details of the LFM and RCM models that are relevant to the present investigation, including the solar wind driving conditions. Section 3 presents the simulation results along with the various spectral analysis techniques that are used to analyze the ULF wave fields. Section 4 discusses the main findings, and in section 5 we offer summarizing and concluding remarks.

2. Model Description and Setup

2.1. The LFM Global MHD Simulation

As the ULF waves under investigation are an MHD phenomenon, the most relevant portion of the simulation is the MHD solver. We discuss the details of the Lyon-Fedder-Mobarry (LFM) code that are the most pertinent for the current study. An in-depth treatment of the numerical methods used therein can be found in *Lyon et al.* [2004].

The LFM model is a state-of-the-art, global, 3-D simulation of the magnetosphere/solar wind interaction. The version of the LFM that is used in this study solves the single-fluid, ideal MHD equations on a nonuniform and nonorthogonal grid that is adapted to study the magnetosphere. In regions of importance for magnetospheric physics, such as the bow shock, magnetopause, and inner magnetosphere, the grid cells are densely packed. The LFM grid that is used here contains $106\times48\times64$ grid cells, which translates to grid cell sizes in the inner magnetosphere on the order of $\frac{1}{4}$ to $\frac{1}{8}$ R_E. Previous work suggests that this grid resolution is sufficient to simulate and resolve important ULF populations in the LFM magnetosphere, including Kelvin-Helmholtz waves and FLRs [*Claudepierre et al.*, 2008, 2010].

The outer boundary condition on the LFM simulation is specified by time series of solar wind plasma and field parameters: magnetic field, velocity, mass density, and temperature. The LFM simulation can be driven by either measured solar wind parameters (e.g., ACE/WIND/ARTEMIS) or by synthetic (e.g., constant or "idealized") solar wind inputs, which can be used to isolate a particular parameter for investigation. The upstream boundary of the simulation is located at $x = 30R_E$, where the solar wind input conditions are prescribed. From this point, the solar wind propagates through the simulation as two-dimensional planar fronts in the antisunward direction. A supersonic outflow boundary condition is used at the rear boundary of the simulation while a ballistic propagation condition is used at the side boundaries.

In this study, we present results from two simulations, one stand-alone LFM and one coupled LFM-RCM. Both simulations are driven by the same idealized fluctuations in solar wind dynamic pressure (p_{dyn}), where we impose a continuum of ULF frequencies in the input number density time series ($p_{\mathrm{dyn}}\sim nv^2$):

$$n(t) = n_0 + \delta n \sum_j \sin\left(\omega_j t + \phi_j\right) \tag{1}$$

In the above equation, we prescribe $\omega_j = 2\pi f_j = 2\pi j/10,000$ and carry out the summation from $j = 1, 2, \cdots, 500$. Thus, the above time series represents a superposition of discrete frequency oscillations over 0 to 50 mHz with a spectral resolution of 0.1 mHz. This input-driving spectrum is imposed on the simulation magnetosphere and serves as a broadband stimulus to which the magnetosphere responds at its natural frequencies of oscillation. A random phase, ϕ_j, is also added to each spectral component. We choose δn so that the RMS of the input time series is roughly equivalent to a 20% oscillation amplitude on top of a background number density of n_0=5 particles/cm^3 (e.g., moderate fluctuation amplitudes). We note that this is the same solar wind driver that was used in [*Claudepierre et al.*, 2010] to study toroidal mode FLRs in the stand-alone LFM.

In the interest of code stability in this numerical experiment and to be as consistent as possible with physical reality, we wish to maintain a pressure balance in the upstream solar wind in the simulations. Thus, we also introduce an oscillation in the input sound speed time series that is out of phase with the number density, resulting in a constant thermal pressure in the upstream solar wind ($p_{\mathrm{th}} \sim nC_s^2$). This out of phase sound speed fluctuation is imposed upon a background value of 40 km/s.

The remaining idealized solar wind input parameters are $\mathbf{B} = (0, 0, +5)$ nT and $\mathbf{v} = (-600, 0, 0)$ km/s, and these values are held constant for the 4 h interval during which the ULF waves are analyzed. We note that synthetic solar wind p_{dyn} fluctuations can be introduced via either the solar wind number density or the velocity, as $p_{\mathrm{dyn}}\sim nv^2$. We impose the p_{dyn} fluctuations via the number density, as solar wind p_{dyn} variations are typically observed to be carried by the solar wind number density, rather than the velocity [e.g., *Kepko and Spence*, 2003; *Han et al.*, 2007]. Moreover, introducing p_{dyn} fluctuations via the velocity components would also introduce an oscillation in the solar wind electric field, complicating the nature of the upstream driver.

For the inner boundary condition in the coupled LFM-RCM model, Poisson's equation is solved to obtain the electric potential in the ionosphere. This calculation is done in a separate module, known as the Magnetosphere-Ionosphere Coupler Solver (MIX) [*Merkin and Lyon*, 2010]. The MIX simulation provides a 2-D electrostatic model of the ionosphere and is two-way coupled to the magnetospheric portion of the simulation (the LFM and the RCM). Once the electric potential is obtained, it is mapped along dipole field lines to a geocentric distance of roughly 2 R_E, where the inner boundary of the LFM simulation is located. The inner boundary condition for the magnetospheric portion of the LFM is then obtained from the electric field computed from the mapped ionospheric potential.

There are two options for the ionospheric conductance model that is used in the MIX potential solver. One is a fixed ionospheric conductance model where a uniform conductance is specified over the entire ionosphere. The other is a more sophisticated representation where an empirical extreme ultraviolet (EUV) conductance model is used. This EUV conductance model includes contributions from particle precipitation and is parameterized by solar EUV flux [*Wiltberger et al.*, 2009]. A similar approach is used in the AMIE model [e.g., *Richmond*, 1992]. In this more sophisticated ionospheric conductance model, the solar EUV flux is regulated by solar 10.7 cm flux, which is a specified input into the MIX ionospheric model. We use this more sophisticated conductance model for the idealized LFM simulations in the current study. However, the 10.7 cm flux value that we choose is somewhat arbitrary, as we are not simulating a particular event or interval. Thus, we use a value of 100 sfu (solar flux unit, 1 sfu = 1×10^{-22} s/m^2), which is the same value used in our previous LFM/ULF studies with which the current simulations will be compared. This choice for the 10.7 cm flux produces a nominal value of 5 mhos for the ionospheric Pedersen conductivity.

2.2. The RCM and Coupling to the LFM

The Rice Convection Model (RCM) is a physics-based model that simulates adiabatically drifting isotropic particle distributions in the magnetosphere. The model, its equations, and numerical methods are tailored for an accurate representation of the particle distributions in the inner magnetosphere. The RCM employs a many-fluid formalism where the particles are represented in terms of multiple fluids. In the stand-alone RCM, the electric fields are computed self-consistently within the RCM using a precomputed, time-dependent magnetic field model that includes the associated induction electric fields. As described below, the coupled LFM-RCM uses the ionospheric electric field supplied by the MIX ionosphere model. The RCM model is thus two-way coupled to the conducting ionosphere, including the flow of electric currents along magnetic field lines, which are assumed to be perfectly conducting. The RCM computes these currents and the associated electric fields self-consistently.

The RCM is an established physical model, and details of the algorithms have been described in various publications [e.g., *Harel et al.*, 1981; *Wolf et al.*, 1991; *Sazykin*, 2000; *Toffoletto et al.*, 2003]. The outer boundary of the model can be placed either as far away from the Earth as possible while still remaining in the region of closed magnetic field lines and sub-Alfvénic flow speed, or it can be positioned at geosynchronous orbit ($L = 6.6$) to take advantage of the particle flux data available. The inner boundary is set at $L = 1.01$ but can be varied as needed. The plasma population is typically represented by 60–150 proton and 25–30 electron isotropic "fluids" (the exact number being run specific) with energy invariants, λ_s, and flux tube content, η_s (s here denotes species). In the LFM-RCM simulation in this study, we use 30 electron fluids and 60 proton fluids. λ_s and η_s are related to the kinetic energy, W_s, and the number density, n_s, through the flux tube volume. The RCM can also track other species such as oxygen and helium. Time steps are typically 1–2 s.

In the coupled LFM-RCM code, the LFM, RCM, and MIX codes run as independent executables and information exchange occurs every minute in simulation time [*Pembroke et al.*, 2012]. The reason for not using a shorter exchange time is that the field line tracing and flux tube volume calculations have to be done at the exchange time cadence. Using a smaller exchange time, for example, something on the order of 10 s, is possible in principle, but anything less quickly renders the simulation intractable, due to the very long run time.

The RCM is initialized assuming a Maxwellian plasma distribution obtained from the LFM and for all other exchanges; only the RCM outer boundary is updated with LFM plasma, while the RCM potential is obtained from MIX. The 3-D, LFM-computed pressures and densities are mapped to the RCM's 2-D ionospheric grid via field line tracing. Using the ionospheric potential computed from the MIX ionosphere model, the RCM then evolves its distribution over the simulation minute. The result is returned to the LFM, which requires an additional field line tracing to map the RCM's 2-D results back onto the 3-D LFM grid. A static plasmaspheric density that depends on L shell and is parameterized by Kp is also added. This is based on a simplified version of the *Gallagher et al.* [2000] plasmaspheric model (henceforth, "GPM") and has the effect adding a cold component of plasma to the inner magnetosphere. These new pressures and densities do not immediately replace the LFM variables but are instead "bled" into the LFM over the exchange time. We note here that the plasmaspheric model is not dynamic; the LFM mass density is continually updated with the GPM value.

2.3. Model Caveats

As described in [*Claudepierre et al.*, 2010], LFM simulations driven by idealized solar wind parameters must be run with an interval of preconditioning prior to the periods selected for ULF wave analysis. In the idealized simulations in the current study, we use the same 5 h IMF preconditioning period that was used in our previous studies: 1 h southward, followed by 1 h northward, followed by 2 h southward, followed by 1 h northward. The IMF magnitude is constant and equal to 5 nT in all of the preconditioning intervals, with no x or y components. The simulations are preconditioned in this manner to impose two intervals of enhanced convection on the magnetosphere, which brings plasma from the tail into the inner magnetosphere. We emphasize that the solar wind dynamic pressure fluctuations are introduced into the simulation after this preconditioning interval and that the IMF is northward during the dynamic pressure fluctuation driving, as described above in section 2.1. Also, the dipole tilt of the geomagnetic field is neglected in the idealized runs under consideration to simplify our analyses and to maintain consistency with our previous idealized LFM studies of ULF pulsations. Similarly, the LFM does not use a rotating dipole. We note that these assumptions of symmetry do affect the distribution of resonant ULF waves in the LFM magnetosphere, and this is discussed further below.

Finally, as discussed in *Claudepierre et al.* [2010], the LFM simulation code uses the "Boris correction" *Boris* [1970], where the perpendicular component of the displacement current is included in the $\mathbf{J} \times \mathbf{B}$ force of the MHD momentum equation but with an artificially low speed of light. In our previous studies of ULF waves in the LFM, this artificial speed of light value was set to 5500 km/s for computational efficiency (e.g., to manage the Courant condition). It was noted that the use of the Boris correction had some influence on the resonant ULF waves under consideration. This is because in the stand-alone LFM, the absence of a plasmasphere results in Alfvén speeds in excess of 5500 km/s in significant portions of the dayside inner magnetosphere (see below). However, the coupled LFM-RCM model contains a realistic mass density profile in the inner magnetosphere, and Alfvén speeds are typically less than 2000 km/s. In the LFM-RCM, the Boris correction only manifests itself in very limited spatial regions of the simulation domain, near the polar ionospheric boundaries, and does not significantly influence the resonant ULF modes under consideration. We note that other global MHD simulations of the magnetosphere, such as BATS-R-US [*Gombosi et al.*, 2003] and OpenGGCM [*Raeder et al.*, 2001] also use the Boris correction.

3. Simulation Results

3.1. Comparisons Between the Stand-Alone LFM and the Coupled LFM-RCM

Figure 1 compares the number density and Alfvén speed profiles in the stand-alone LFM (henceforth, "LFMbase") and the coupled LFM-RCM (henceforth, "LFMrcm") simulations, driven by the identical, quasi-broadband solar wind inputs described above. We emphasize that the LFMbase simulation presented here is the same simulation that was used in the toroidal mode FLR study of *Claudepierre et al.* [2010]. Figure 1a shows the logarithm of the number density in the GSM equatorial plane from the LFMbase simulation averaged over the 4 h duration of the simulation (GSM coordinates are used throughout this study). Figure 1b shows the same quantity from the LFMrcm simulation and Figure 1c compares the radial profiles of the number density along the 09 MLT meridian from both simulations. In Figures 1a and 1b, a snapshot of the magnetopause is shown as the white contour that intersects the noon meridian at roughly 10 R_E. The bow shock can be seen as the sharp gradient in number density a few R_E anti-earthward of the magnetopause. In Figure 1c, the approximate location of the magnetopause along 09 MLT in each simulation is indicated by the vertical dashed traces labeled "MP." In addition, for the LFMrcm simulation, the approximate location of the plasmapause is indicated by the vertical dashed trace labeled "PP." In Figure 1c, note that from approximately 1 R_E earthward of the magnetopause out into solar wind, the radial profiles of the number densities are nearly identical in the two simulations, apart from a small horizontal shift. This represents the fact that two simulations are driven by the same solar wind conditions. The small horizontal shift is due to the slightly inflated magnetosphere in the LFMrcm, a result of a slightly enhanced ring current pressure, via the inclusion of the RCM in the coupled model (on the dayside, the LFMrcm thermal pressure is roughly a factor of 2–3 times greater than that of the LFMbase). If these simulations were driven with southward IMF, the inflation in the LFMrcm would be more pronounced as the RCM ring current would be enhanced when compared with the weak ring current produced in the LFMbase [*Pembroke et al.*, 2012].

In Figures 1b and 1c, the inclusion of the GPM in the LFMrcm is clear, with a sharp plasmapause boundary at $r \approx 4.8\ R_E$ and dense plasmaspheric material earthward of this location. For this simulation, Kp was fixed at 3 in the static GPM, which produces a somewhat eroded plasmasphere, representative of moderate geomagnetic

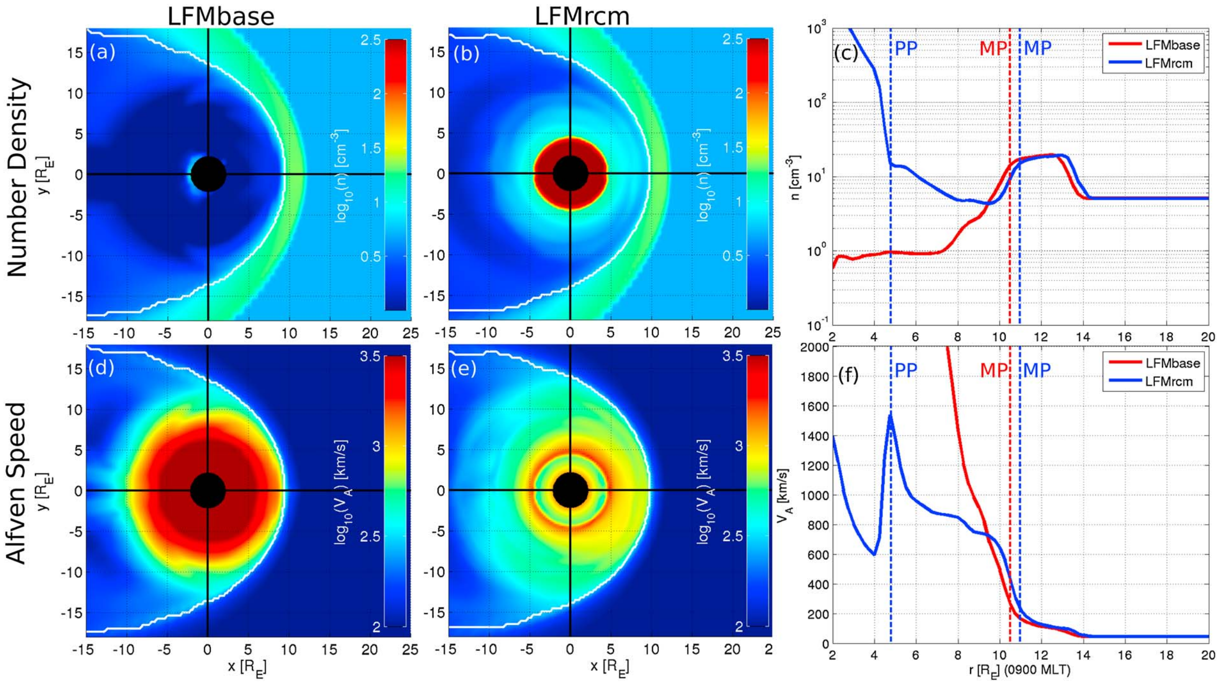

Figure 1. Comparison of the (a–c) number density and (d–f) Alfvén speed profiles in the stand-alone LFM (LFMbase) and coupled LFM-RCM (LFMrcm) simulations. Figures 1a, 1b, 1d, and 1e display these quantities in the equatorial plane on a logarithmic color scale. Note the extremely low density values in the stand-alone LFM (Figure 1a) in the inner magnetosphere, which results in extremely large Alfvén speed values in the inner magnetosphere (Figure 1d). The coupled LFM-RCM model, which includes a plasmasphere, does not suffer from this shortcoming (Figures 1b and 1e), and the number density and Alfvén speed values are more representative of the real magnetosphere. Figures 1c and 1f compare the number density and Alfvén speed profiles along the 0900 MLT meridian in the two simulations, where the magnetopause (MP) and plasmapause (PP) boundaries are indicated.

activity. Also note the region of elevated plasma density extending several R_E just outside of the plasmapause, particularly clear in Figure 1b, which is a plasmatrough-like feature of the LFM-RCM (this feature is not part of the empirical GPM). The plasmaspheric influence on the 4 h averaged Alfvén speed (v_A) profiles, shown in Figures 1d–1f, is also clear, as $v_A \sim B/\sqrt{n}$. We emphasize the extraordinarily large values of the Alfvén speed (off scale) in the inner magnetosphere in the LFMbase, due to the absence of any significant mass density inside of $r \approx 9\ R_E$. The radial profile of the Alfvén speed shown in Figure 1f from the LFMrcm simulation (blue trace) is much more representative of the real magnetosphere than what is obtained from the LFMbase simulation (red trace). Throughout this work, we define the plasmapause as in *Takahashi et al.* [2010] as the local maximum of the Alfvén speed profile (e.g., Figure 1f).

3.2. Spectral Analysis

The output from the magnetospheric portion of the LFM simulation gives the MHD variables (vector magnetic field, vector velocity field, mass density, and temperature) and various derived quantities (e.g., vector electric field and vector current density) at every grid point in the simulation domain. In this work, we focus on ULF pulsations in the E_φ and $B_{||}$ field components, as these are the most relevant for interactions with radiation belt electrons [*Northrop*, 1963]. ULF pulsations in E_r are also considered, due to their role in resonant mode coupling. Spectral analyses are performed on the simulated time series to characterize any ULF pulsations present. We compute the power spectral density (PSD) via the multitaper method [*Thomson*, 1982; *Percival and Walden*, 1993] at a sampling rate of 10 s, sufficient to accurately resolve Pc4–5 ULF waves. We do not perform any filtering on the time series prior to the application of the spectral estimator; the only preconditioning done is a mean removal.

Figure 2 shows radial profiles of PSD along the 09 MLT meridian (horizontal scale) versus frequency (vertical scale), with wave power plotted on a logarithmic color scale. The vertical dashed line near 10 R_E indicates the approximate location of the magnetopause (MP). Figure 2a shows the PSD profile of the radial electric field, E_r, with solid white traces overlaid that show estimates of the local field line eigenfrequencies along the 09 MLT meridian. These eigenfrequencies are obtained by numerically solving the toroidal mode wave equations using the Alfvén speed profiles from the simulation. For comparison, an approximate, closed

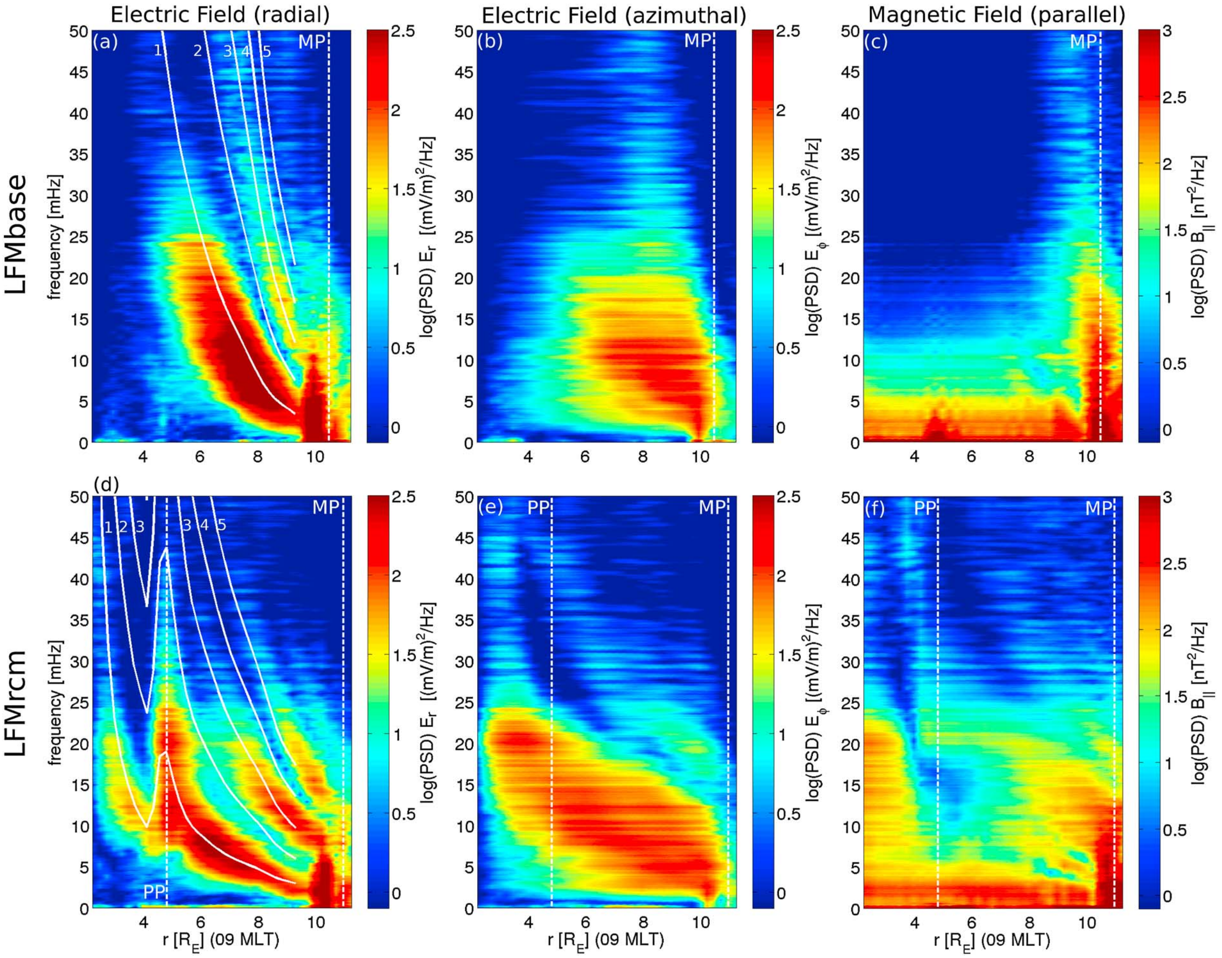

Figure 2. Resonant mode coupling between the fast compressional mode and shear Alfvén mode in the (a–c) LFMbase and (d–f) LFMrcm simulations. In each panel, wave fluctuation amplitude is plotted on a logarithmic color scale for fluctuations in the 0–50 mHz ULF frequency range (vertical scale) versus radial distance along the 0900 MLT meridian (horizontal scale). Three simulated field components are shown: The radial electric field (E_r, Figures 2a and 2d), the azimuthal electric field (E_φ, Figures 2b and 2e), and the parallel magnetic field ($B_{||}$, Figures 2c and 2f). The fluctuations in E_r are the signature of toroidal mode FLRs excited in the dayside and track the odd-mode harmonic field line eigenfrequency profiles (solid white traces) computed from the field-aligned Alfvén speed profiles in the simulations. The fluctuations in E_φ and $B_{||}$ are the signature of fast compressional mode waves that are launched near the subsolar magnetopause. Note the radial eigenmode structure, characteristic of a resonant cavity or waveguide: At the spatial locations where E_φ has an oscillation amplitude node, $B_{||}$ has an antinode, and vice versa (e.g., Figures 2d and 2f). The inclusion of a plasmasphere in the LFMrcm simulation clearly has a significant impact on the ULF waves. For example, the compressional mode waves in E_φ in the LFMrcm penetrate deeper (more earthward; Figure 2e), thus coupling their energy into the FLRs at more earthward locations (Figure 2d), when compared with the LFMbase (Figures 2a and 2b). The spatially uniform regions of $B_{||}$ wave power below ~5 mHz in both simulations (Figures 2c and 2f) are identified as a quasi-static breathing mode signature. The magnetopause (MP) and plasmapause (PP) locations along the 0900 MLT meridian are indicated by the vertical, white dashed lines.

form expression for the full wave equation solution can be obtained via a WKB method, which is essentially the Alfvén time-of-flight integral along the field lines that intersect the 09 MLT meridian in the equatorial plane:

$$f_n = n\left[2\int_S^N \frac{\mathrm{d}s}{v_A(s)}\right]^{-1} \quad \text{for } n = 1, 2, 3, \ldots \tag{2}$$

Here the integration is carried out along the field line of interest, from the southern field line foot point (S) to the northern foot point (N). The labels "1,...,5" in Figure 2a indicate the harmonic number, n, of the field line eigenfrequency (e.g., $n = 1$ is the fundamental, $n = 2$ is the second harmonic, etc.). We emphasize the notational ambiguity here, where we have used n for the FLR harmonic number, while in section 2, n was used to represent the plasma number density. Note the two regions of enhanced E_r wave power that closely track the $n = 1$ and the $n = 3$ eigenfrequency traces. These are the signatures of the fundamental and $n = 3$ toroidal mode FLRs excited along the 09 MLT meridian [see *Claudepierre et al.*, 2010]. Due to the nature of the solar wind propagation as planar fronts and the zero-dipole tilt angle used in this simulation, only odd mode number

FLRs are excited. This is consistent with theoretical expectations for zero-dipole tilt and previous modeling work [*Lee and Lysak*, 1991].

Figure 2b shows the PSD profile of the azimuthal electric field, E_φ, along the 09 MLT meridian, while Figure 2c shows the PSD profile of the compressional magnetic field, $B_{||}$. A set of plots analogous to Figures 2a–2c is shown in Figures 2d–2f where an additional vertical dashed trace near $r = 4.8\ R_E$ indicates the approximate location of the plasmapause (PP). Comparing Figures 2a–2c with the analogous Figures 2d–2f shows that even the inclusion of the simple, static GPM plasmasphere in the LFMrcm has a profound impact on the simulated ULF waves. The pertinent features in these panels are discussed in greater detail in section 4. For completeness, in the supporting information we show analogous plots from the LFMrcm simulation for the remaining electric and magnetic field components (B_r, B_φ, and $E_{||}$), where the fluctuations are found to be negligible.

We note that two of the LFMrcm coupling techniques described above, the location of the RCM boundary (at roughly 8.5 R_E along the 09 MLT meridian in this simulation) and the LFMrcm exchange time (1 min = 16.7 mHz) do not manifest themselves in Figures 2d–2f. In particular, the spectra are continuous across both 8.5 R_E and 16.7 mHz, suggesting that the location of the RCM boundary and the LFMrcm exchange time do not influence the simulated ULF waves. We also note that the spatial discretization and the nature of the numerical schemes used in the LFM simulation results in a filtering of higher-frequency spectral components ($f > 25$ mHz) in the upstream solar wind in these simulation. This is to be expected and explains why the magnetospheric response decays sharply for $f > 25$ mHz in Figure 2 (see *Claudepierre et al.* [2009, 2010] for more detailed discussions of this point).

Figure 3 shows maps of ULF wave power in the GSM equatorial plane, which provide a more global context than the radial profiles shown in Figure 2, but without the detailed spectral information. These maps are constructed by recording the time series of interest at every grid point in the equatorial plane, computing the PSD of the time series and then calculating the root-integrated power (RIP) of the PSD over a given frequency band of interest $[f_a, f_b]$:

$$\mathrm{RIP} = \left[\int_{f_a}^{f_b} \mathrm{PSD}(f)\mathrm{d}f\right]^{\frac{1}{2}} \tag{3}$$

Thus, RIP is a measure of the fluctuation amplitude in the frequency range $[f_a, f_b]$ and has the same units as the time series analyzed. In Figure 3, RIP is shown on the color scale integrated over the frequency range $[f_a, f_b] = [0.5,50]$ mHz. In Figures 3a–3c, three field components from the LFMbase simulation are shown in each row: E_r, E_φ, and $B_{||}$, respectively. Figures 3d–3f show the analogous set of plots from the coupled LFMrcm. A snapshot of the magnetopause is shown in each panel as the black contour that intersects the noon meridian at roughly 10 R_E. The bow shock can be seen as the region of enhanced wave power anti-earthward of the magnetopause. In addition, in Figures 3d–3f, a snapshot of the plasmapause is shown as the black, roughly circular contour near 4.8 R_E. This contour is specified at the number density value of 15 particles/cm^3 (e.g., Figure 1c). Again, for completeness, in the supporting information we show analogous plots from the LFMrcm simulation for the remaining electric and magnetic field components (B_r, B_φ, and $E_{||}$), where the fluctuations are found to be negligible. Finally, we note the absence of wave power in the solar wind, as these idealized simulations are driven solely by a fluctuating solar wind p_{dyn}, with the fluctuations carried by the number density.

In Figure 3, as in Figure 2, there are several differences between the LFMbase and LFMrcm simulation results. In Figure 3a, the toroidal mode FLR wave power is stronger and is more spatially uniform when compared with the profiles shown in Figure 3d from the LFMrcm. In Figure 3d, note the spatially distinct regions of FLRs: There is one resonant L shell outside of the plasmasphere, another resonant L shell immediately adjacent to the plasmapause, and a third resonant L shell, with a weaker amplitude, entirely within the plasmasphere. Comparing Figures 3b and 3e, we note that the E_φ wave power profiles look quite similar near the subsolar magnetopause where the compressional waves are generated. However, in the LFMrcm, the wave power extends farther earthward, all the way into the dayside plasmasphere. The spatial distribution of compressional magnetic field power in the dayside is also different between the two simulations and is discussed further below. Finally, we note the ring of enhanced wave power in Figure 3c near 5 R_E that is likely a numerical artifact in the LFMbase simulation, related to the spatial discretization. This grid artifact can also be seen near 5 R_E in Figure 2c.

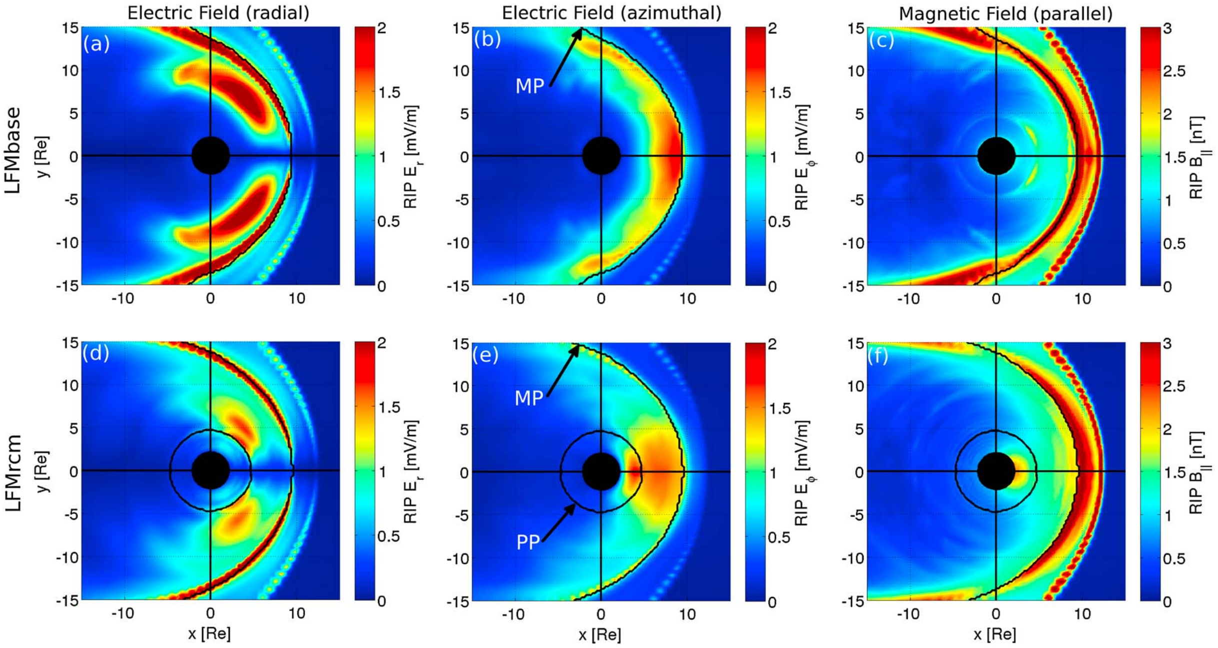

Figure 3. Wave fluctuation amplitude in the equatorial plane from the (a–c) LFMbase and (d–f) LFMrcm simulations. These provide a more global context for the ULF oscillations excited by the upstream dynamic pressure fluctuations, when compared with the radial profiles revealed in Figure 2. However, these panels lack the detailed spectral information shown in Figure 2, as each panel shows ULF wave power integrated over the 0.5–50 mHz ULF frequency range. Three simulated field components are again shown: E_r (Figures 3a and 3d), E_φ (Figures 3b and 3e), and $B_{||}$ (Figures 3c and 3f). Figures 3a and 3d show the absence of toroidal mode FLRs near the noon meridian, due to the symmetry of the upstream driver. Figures 3b and 3e show the deeper penetration (more earthward) of the compressional electric field oscillations in the LFMrcm, when compared with the LFMbase. Figures 3a, 3b, 3d and 3e also suggest the resonant waveguide character of the magnetosphere, as the wave power is most intense on the dayside and attenuates strongly on the nightside. The magnetopause (MP) and plasmapause (PP) locations are shown in all six panels, with labels in Figures 3b and 3e.

4. Discussion

4.1. Resonant ULF Mode Coupling

Claudepierre et al. [2010] described the dayside fluctuations in the radial electric field, E_r, shown in Figures 2a and 3a as the signature of toroidal mode FLRs excited by the quasi-broadband upstream p_{dyn} fluctuations. In addition, in Figure 2a, note that the $n = 1$ toroidal mode wave power is most intense between ~7–9 R_E on the 09 MLT meridian (deep red). The local maximum in wave power at this location is due to coupling from the compressional mode, which is shown in Figure 2b. Here note that the compressional mode E_φ wave power is most intense near 10 mHz and decays rapidly away from the magnetopause, earthward of 6 R_E. The frequency selection in the compressional mode is due to the resonant cavity/waveguide nature of the magnetosphere [*Claudepierre et al.*, 2009] and explains why the FLRs are the strongest between 7–9 R_E. At this location, the local field line eigenfrequency is roughly 10 mHz (Figure 2a, $n = 1$) and the coupling of compressional mode energy into the FLR is strongest. This resonant mode coupling behavior can also be seen in Figure 3a as the radially localized peaks in toroidal mode FLR wave power near $r = 7–9$ R_E present throughout most of the dayside. Also, as discussed in *Claudepierre et al.* [2010], the absence of toroidal mode FLRs near the noon meridian in Figure 3a is due to the symmetric nature of the solar wind driving, where *yz* planar fronts impact the subsolar magnetopause.

As noted above, the presence of a cold, dense plasmasphere in the coupled LFMrcm, and to a lesser degree the elevated plasma density beyond the plasmapause, has a dramatic impact on the simulated ULF waves. For example, in Figure 2d, note that the locations of the toroidal mode FLRs have shifted earthward, when compared with the locations in the LFMbase (Figure 2a). This is due to the increased plasma density in the dayside magnetosphere in the LFMrcm, which has the effect of reducing the Alfvén speed and thus reducing the resonant frequency at a given radial location. This earthward shift, which leads to more harmonics in the LFMrcm simulation, can also be seen by comparing the eigenfrequency traces in Figure 2a with those in Figure 2d. Also, note that the profile of the fundamental mode FLR changes dramatically at the plasmapause in the LFMrcm ($n = 1$, Figure 2d), with strong toroidal mode wave power excited over a wide range of frequencies at the plasmapause. This broadband toroidal mode wave power near the plasmapause could be due to a number of factors: a significant amount of phase mixing at the boundary [*Wright et al.*, 1999], plasmapause surface waves [*Chen and Hasegawa*, 1974b], a leaky boundary interface between two cavities [*Allan et al.*, 1986b], or strong resonant mode coupling at the plasmapause. A thorough evaluation of these possibilities is warranted, but we do not present one here. We also see a region of enhanced wave power inside the plasmasphere, which is the signature of the fundamental toroidal mode FLR within the plasmaspheric cavity. Furthermore, comparing Figures 2a and 2d reveals that the resonance widths are slightly different between the two simulations. We find that the resonance widths (the full width at half maximum) in the LFMbase are on the order of 1.1 R_E, while in the LFMrcm they are slightly wider, at about 1.3 R_E (please refer to Figure S4 in the supporting information for a comparison of the resonance widths in the two simulations). We hesitate to ascribe any physical meaning to this difference in widths, as it is on the order of 2 grid cells. Additional analysis using simulations with a finer grid resolution would need to be conducted to investigate this further, but this is beyond the scope of the present study.

In Figure 2e, the radial profile of compressional mode electric field, E_φ, wave power is also considerably different than that in the LFMbase simulation. The compressional waves are able to penetrate deeper into the magnetosphere in the LFMrcm, again due to the increased mass density in this model. Note also that in the LFMrcm simulation, we see the presence of compressional mode wave power inside the plasmasphere.

In both Figures 2b and 2e, it is clear that the penetration depth of the compressional waves is a function of frequency, where the higher-frequency waves penetrate farther earthward. This can be understood by considering that in a magnetospheric waveguide, the radial location of the turning point, $r_{\rm tp}$, must satisfy the following relation [*Samson et al.*, 1992; *Wright*, 1994]:

$$\omega^2 = v_A^2(r_{\rm tp})\left[k_\varphi^2 + k_{||}^2\right] \tag{4}$$

where ω is the wave frequency, and k_φ and $k_{||}$ are the azimuthal and field-aligned wave numbers, respectively. We can calculate the predicted location of the turning points directly from the Alfvén speed profiles in each simulation. Using $k_\varphi = m/r$, where m is the azimuthal mode number and $k_{||} = \pi/a$ (for the fundamental mode), where $a = a(r)$ is the field line length as a function of radial distance, r, equation (4) becomes:

$$\omega^2 = v_A^2(r_{\rm tp})\left[\left(\frac{m}{r_{\rm tp}}\right)^2 + \left(\frac{\pi}{a(r_{\rm tp})}\right)^2\right] \tag{5}$$

$$2\pi f = v_A(r_{\rm tp})\sqrt{\left(\frac{m}{r_{\rm tp}}\right)^2 + \left(\frac{\pi}{a(r_{\rm tp})}\right)^2} \tag{6}$$

We now demonstrate how we solve for the turning point locations, $r_{\rm tp}$, along the 09 MLT meridian, using the LFMrcm simulation results as an example. We extract from the simulation the Alfvén speed profile ($v_A(r)$) and the field line length profile ($a(r)$), both terms which appear on the right-hand side of equation (6). Using these terms, we obtain the blue trace in Figure 4a: The profile of the right-hand side of equation (6) along the 09 MLT meridian from the LFMrcm simulation for fixed azimuthal mode number, $m = 1$. The horizontal red trace shows the left-hand side of equation (6) for a fixed frequency, $f = 10$ mHz. The intersection points of these two curves thus gives the location of the turning point along the 09 MLT meridian (in this case, $r_{\rm tp} = 5.4\ R_E$). We repeat this calculation for each frequency f from 0 to 50 mHz and we assume $m = 1$. While we assume $m = 1$ for simplicity, it is possible to compute the azimuthal mode number spectrum directly from the LFM simulation [e.g., *Claudepierre et al.*, 2008]. This is beyond the scope of the present study, but initial calculations suggest that $m < 5$, with peak power in the $m = 1$–2 range in both simulations. These calculations, along with a detailed analysis of the wave polarizations, will be presented in follow-on work.

The resultant profiles of $r_{\rm tp}$ are plotted as red dotted traces in Figure 4b for the LFMbase simulation and in Figure 4c for the LFMrcm simulation. For the LFMrcm simulation, when there are multiple intersection points due to the presence of a plasmasphere (as in Figure 4a), we use the largest value of $r_{\rm tp}$ as the turning point location. In Figures 4b and 4c, E_φ PSD is shown on the color scale and the plots are identical to Figures 2b and 2e except that we have changed the range on the color scale to emphasize the comparison with the turning point profiles. Here we see good agreement between the estimated turning point profiles computed from the simulated Alfvén speed profiles and the frequency-dependent penetration depth of the compressional waves.

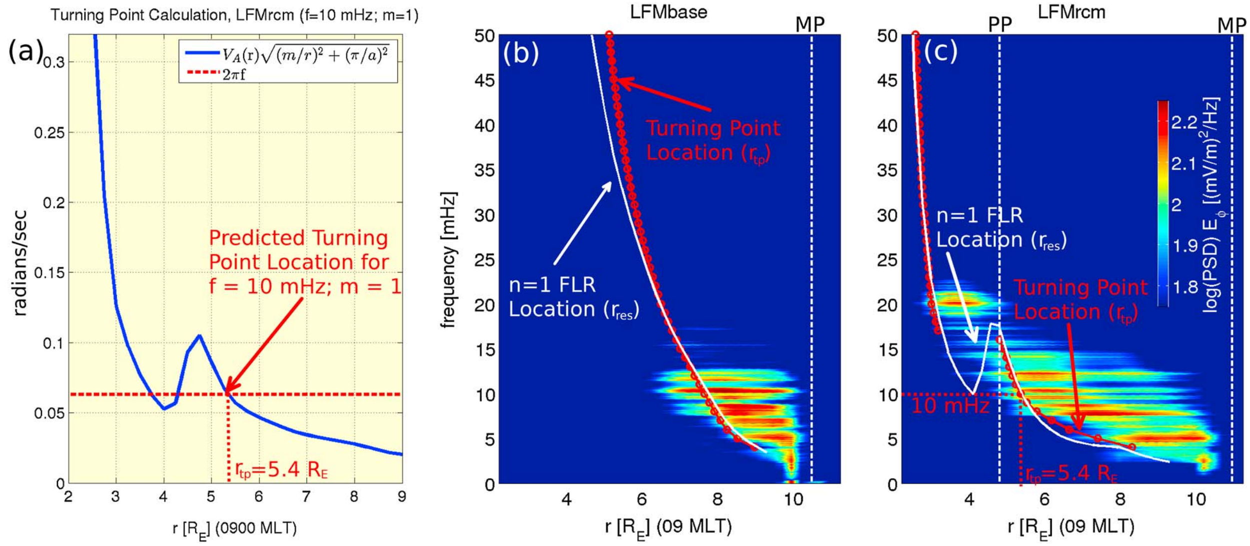

Figure 4. Turning point locations (r_{tp}) calculated from the Alfvén speed profiles from the LFMbase and LFMrcm simulations. (a) An example of this calculation for a frequency, f, of 10 mHz and azimuthal mode number, m, of 1, where we find $r_{\text{tp}} = 5.4\ R_E$. (b) The turning point location profile obtained by this procedure in the LFMbase simulation (red dotted trace). The radial profile of the $n = 1$ FLR is also shown (e.g., Figure 2a) as the white trace, for comparison. Azimuthal electric field wave power along the 0900 MLT meridian is shown on the logarithmic color scale and is identical to Figure 2b aside from a different range on the color scale. (c) The analogous information from the LFMrcm simulation. In Figures 4b and 4c, note that the compressional mode electric field oscillations penetrate earthward to (roughly) the predicted turning point location, beyond which the mode becomes evanescent and couples its energy in the FLR. This behavior is characteristic of a resonant waveguide. Also, note that higher-frequency fluctuations penetrate deeper than lower frequency fluctuations, due to the radial dependence of the turning point profiles. Similarly, the inclusion of a plasmasphere in the LFMrcm (Figure 4c) leads to a deeper penetration of the compressional electric field fluctuations when compared with the LFMbase (Figure 4b).

At higher frequencies, the predicted turning point locations are at lower radii, consistent with the wave behavior in the simulations. In Figures 4b and 4c, we also show, for comparison, the $n = 1$ FLR profiles from Figures 2a and 2d. The turning point and FLR profiles are essentially indistinguishable, when the grid resolution of the simulation is considered, which indicates that the fast mode is easily able to reach the resonance location [e.g., *Wright*, 1994]. We also note that the FLRs in the LFMbase and LFMrcm show an approximately 180° phase reversal across the amplitude peak, as expected from resonant mode coupling theory (see Figure S4 in the supporting information), which is also similar to what was found in the LFMbase simulations of *Claudepierre et al.* [2010]. Returning to the figure, Figure 2c shows the PSD of the compressional magnetic field, $B_{||}$, in the LFMbase simulation. Note that the $B_{||}$ wave power is strong below roughly 5 mHz and does not show any appreciable spatial structure within the simulation magnetosphere. Figure 2f shows the analogous wave power profile from the LFMrcm simulation. Again, below ~5 mHz, the wave power is strong and is uniform in space. The absence of spatial structure in the compressional magnetic field oscillations below 5 mHz cannot be explained by resonant cavity oscillations at these frequencies, as resonant radial eigenmodes have a nodal/antinodal structure (see section 4.2). Instead, we argue that the $B_{||}$ oscillations below 5 mHz are the signature of the quasi-static breathing mode [e.g., *Takahashi and Ukhorskiy*, 2007]: Fluctuations at these frequencies have periods longer than the Alfvén travel time across the dayside magnetosphere. Thus, the compressional magnetic field in the magnetosphere responds to the upstream p_{dyn} fluctuations below ~5 mHz via a quasi-static, forced oscillation [*Kepko and Spence*, 2003]. This particular value of 5 mHz for the cutoff frequency is strongly influenced by the Alfvén speed profiles in the simulations (and also the Boris correction in the LFMbase) and, as such, may not be directly comparable to the real magnetosphere. Future work will investigate the sensitivity of this value to a dynamically evolving plasmasphere and thus a dynamically evolving Alfvén speed profile.

It is interesting to note that the LFMrcm magnetosphere appears to support much stronger compressional magnetic field oscillations than the LFMbase, above 5 mHz. One possible explanation is that the outer resonant cavity region (the plasmapause to magnetopause) is smaller in the LFMrcm than it is in the LFMbase (the inner boundary to the magnetopause). However, we do not, at this time, have a definitive explanation for the weak $B_{||}$ fluctuations above 5 mHz in the LFMbase simulation.

Finally, we have argued above that the inclusion of the GPM is the primary factor that influences the simulated ULF wave fields in the LFMrcm, when compared with the LFMbase. There are, however, other differences between the two models that could also potentially lead to the ULF wave differences highlighted above. First, the elevated plasma density beyond the plasmapause seen in Figure 1 also influences the simulated ULF waves, much in the same way that the inclusion of the plasmasphere does. While this plasmatrough-like feature is not part of the GPM, it would certainly not be present in the LFMrcm if the GPM were not included. Thus, while the inclusion of the GPM does lead to the plasmatrough-like feature in the LFMrcm, this feature alone cannot explain all of the ULF wave differences noted above and certainly not those within the plasmasphere region.

Second, while the RCM itself does not support wave propagation, there is additional physics in the LFMrcm that is not included in the LFMbase that could also potentially impact the simulated ULF waves. The primary factor of note here is the ring current drift physics of the RCM and the impact that this has on the thermal pressure distribution in the inner magnetosphere. Previous studies have shown that increasing the thermal pressure/plasma beta can alter the ULF mode structure and lead to a more earthward energy transport [*Kouznetsov and Lotko*, 1995] similar to the effects attributed to the inclusion of a plasmasphere in this study. However, as noted above, the pressure differences between simulations are small (on the order of factors of 2 to 3). Thus, we argue that the inclusion of the plasmasphere, rather than finite thermal pressure effects, is the primary factor that leads to the differences noted in the resonant ULF mode coupling. In addition, note that the results presented here agree very well with cold plasma theory, further substantiating this assertion. Furthermore, we emphasize that the simulations presented in this study are conducted under northward IMF, where the ring current is suppressed when compared with southward IMF simulations. Thus, the potential effects of larger plasma pressures on ULF wave fields may be important for future studies using LFMrcm simulations. For example, the results presented here could differ significantly from new LFMrcm simulations that use the same plasmasphere model but with different pressure/plasma beta outside of the plasmasphere [cf. *Kouznetsov and Lotko*, 1995].

4.2. Radial Eigenmodes

Above, we argued that the simulated ULF waves are consistent with resonant mode coupling theory, where the compressional waves launched at the magnetopause propagate earthward until the turning point is reached, beyond which they transfer energy into the local FLR. In a resonant cavity such as this, the compressional oscillations in the wave electric and magnetic fields should exhibit a standing wave structure in the radial direction. For example, in Figures 2e and 2f, note that the spatial locations where the compressional magnetic field oscillations are the strongest correspond to the locations where the compressional electric field oscillations are the weakest, and vice versa. This nodal/antinodal structure is the signature of a cavity-/waveguide-type radial eigenmode.

To further investigate this nodal/antinodal structure in the LFMrcm simulation, we compute radial profiles of RIP (equation (3)) in various frequency bands along the noon meridian. Figure 5 shows such profiles for the compressional electric field, E_φ, in black, and the compressional magnetic field, $B_{||}$, in red. Figure 5a shows the RIP integrated over 0.5–50 mHz, which is the same range used in the equatorial plane wave power maps shown in Figure 3. Thus, the black and red profiles in Figure 5a can be directly compared with Figures 3e and 3f along the noon meridian.

In Figure 5a, the magnetic and electric field amplitude profiles do not show any appreciable spatial structure, apart from gradients in wave power near the natural boundaries of the system: the ionosphere (inner boundary), plasmapause (PP), magnetopause (MP), and bow shock (BS). In Figures 5b–5g, we partition the 7 to 50 mHz frequency band into six RIP bands of 7 mHz bandwidth each (e.g., 7–14 mHz, 14–21 mHz, etc.). We only consider fluctuations above 7 mHz because the response is nonresonant below this frequency (the breathing mode—see above). Figures 5b–5g reveal the expected radial eigenmode structure: Where the magnetic field oscillation has a node, the electric field oscillation has an antinode, and vice versa.

The simulation results presented suggest that the plasmapause forms a natural boundary that reflects and transmits wave energy. In particular, the eigenmodes are well developed within the plasmaspheric cavity, with one electric field antinode in Figures 5c and 5d that evolves into two antinodes at higher frequencies (e.g., Figure 5g). Similarly, in the magnetosphere, between the plasmapause and magnetopause, the electric field has one antinode in Figure 5b, two in Figure 5d, and three in Figure 5f, though the eigenmode structure

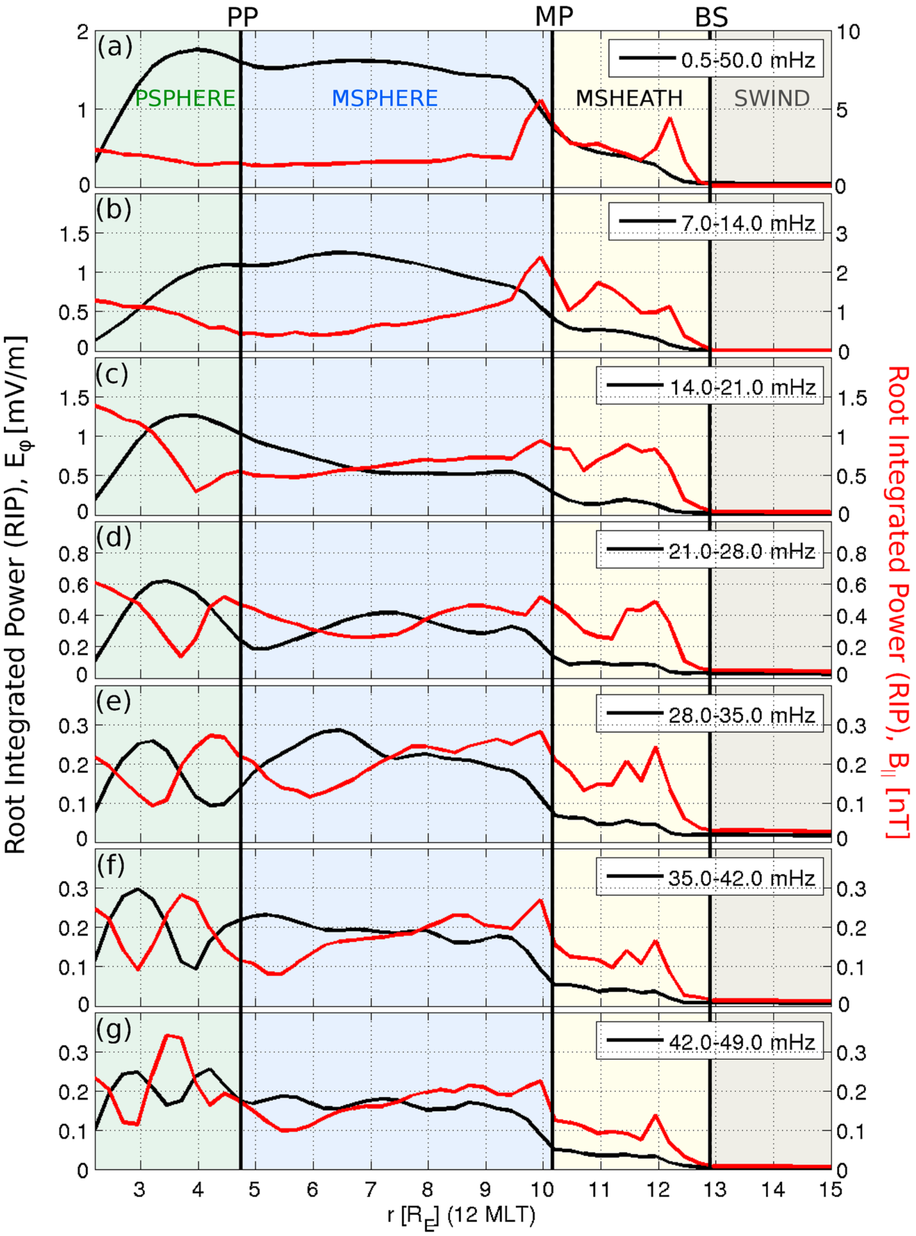

Figure 5. Radial eigenmode structure for the fast compressional mode along the 1200 MLT meridian in the LFMrcm simulation. In each panel, root-integrated wave power (RIP) is shown integrated over various frequency bands for the compressional electric field, E_φ (black), and the compressional magnetic field, $B_{||}$ (red). (a) RIP integrated over 0.5–50 mHz (e.g., compare with Figures 3e and 3f). (b–g) We partition the 7 to 50 mHz frequency band into six RIP bands of 7 mHz bandwidth each (e.g., 7–14 mHz, 14–21 mHz, etc.). Note the radial standing waves within both the plasmasphere (PSPHERE) and the magnetosphere (MSPHERE) in Figures 5b–5g, with higher harmonics at higher frequencies.

in the magnetosphere is less clear than in the plasmasphere. This may be related to the grid resolution in the simulation, as the grid resolution increases closer to the inner boundary (i.e., as *r* decreases).

The radial eigenmode structure described here is analogous to what was found in the work of *Claudepierre et al.* [2009], where the LFMbase simulation was used to simulate cavity modes under similar driving conditions. We argue that the resonant magnetospheric cavity is more properly interpreted as a waveguide, as the compressional mode wave energy ultimately escapes to the nightside, where it is dissipated downtail through the system. A scientific visualization is presented in the supporting information that supports this interpretation of the energy flow. Furthermore, the global maps of compressional wave power presented in Figures 3b,

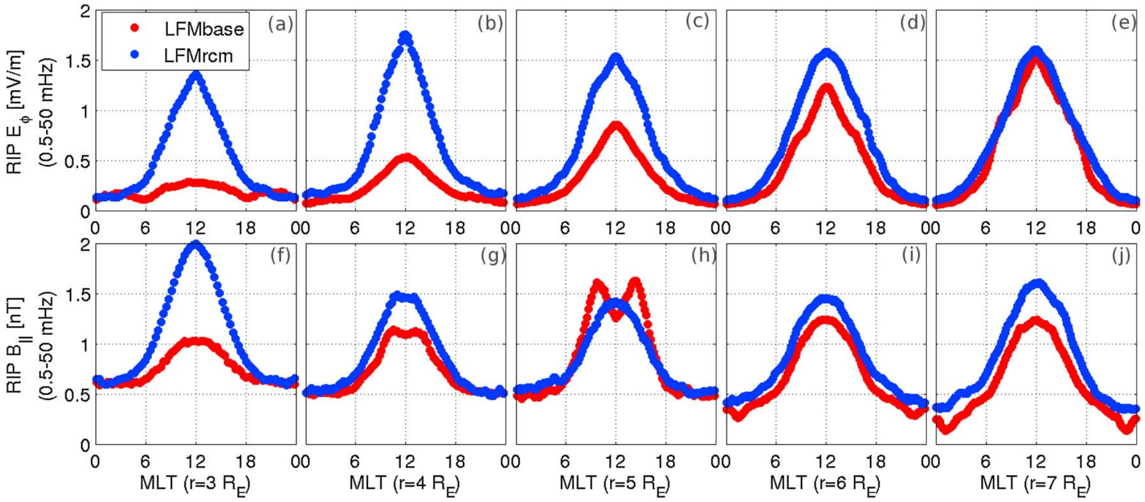

Figure 6. Azimuthal (MLT) profiles of root-integrated power (RIP) at five fixed radial locations (columns; $r = 3$, 4, 5, 6, and 7 R_E) for the (a–e) azimuthal electric field (E_φ) and the (f–j) parallel magnetic field ($B_{||}$). These field components are the most relevant for drift-resonant interactions with energetic (e.g., hundreds of keV) radiation belt electrons. In each panel, RIP is integrated over 0.5–50 mHz and the LFMbase (red) is compared with the LFMrcm (blue) simulation. Note that at lower radial locations, in the heart of the radiation belt region (e.g., $r = 3$–4 R_E, Figures 6a, 6b, 6f, and 6g), the wave power in the LFMrcm is stronger than that in the LFMbase simulation. Such considerations are important for radiation belt modeling, as the radial transport rates computed from such simulated wave fields will differ between the LFMbase and the LFMrcm simulations (the radial diffusion coefficient is proportional to the ULF fluctuations in this frequency range). The inclusion of the plasmasphere in the LFMrcm is the primary factor that leads to these differences in simulated wave amplitudes.

3c, 3e, and 3f also support this interpretation of a loss of energy through to the nightside. Here we see that the wave power is most intense on the dayside, and as the waves propagate through to the nightside, they dissipate and the amplitude decreases. The resonant waveguide interpretation is further supported by the turning point analysis presented above.

4.3. Implications for Radiation Belt Modeling

As discussed in section 1, in MHD test particle simulations of the radiation belts, the rates of electron radial transport are determined directly by the MHD-simulated electric and magnetic fields. If the ULF wave frequency, ω, is not modeled accurately in such simulations, then the MHD test particle tracing will produce particle transport at the incorrect energy, as the particle energy is proportional to the drift frequency, ω_d, via the drift resonance condition, $\omega = m\omega_d$. Conducting full MHD test particle simulations is beyond the scope of the current work. However, from the analyses presented above, it is readily apparent that the inclusion of a plasmasphere in the global MHD model has a substantial impact on the physical characteristics of the simulated ULF waves. For example, comparing Figures 2a–2c with Figures 2d–2f shows that the simulated wave frequencies are strongly influenced by the presence of the plasmasphere. Furthermore, these panels show that there is a large difference in the penetration depth of the compressional electric field fluctuations between the two simulations. In the LFMbase, the fluctuations are confined to larger radial distances, outside of the heart of the outer electron radiation belt (e.g., $L=3$–5). However, in the LFMrcm model, the compressional electric field fluctuations are able to penetrate deep into the radiation belt region. Thus, in MHD test particle simulations, one would expect to find both electron transport to lower L in the LFMrcm and at different resonant energies in the LFMrcm, when compared with the LFMbase.

Furthermore, an azimuthally drifting electron will sample the wave electric field over its entire drift orbit [*Elkington et al.*, 2003]. Again, from the above analyses, it is clear that this sampling will be significantly different between the LFMbase and LFMrcm. To demonstrate this, Figure 6 shows azimuthal (i.e., MLT) profiles of RIP wave power (0.5–50 mHz) in the compressional electric (Figures 6a–6e) and magnetic fields (Figures 6f–6j). These profiles are shown at five fixed radial distances, $r = 3$, 4, 5, 6, and 7 R_E (columns), for both the LFMbase (red) and LFMrcm (blue) simulations. In the outer portions of the radiation belt region, $r = 6$–7 R_E, the wave intensities are roughly comparable between the LFMbase and LFMrcm simulations. However, further earthward, into the heart of the radiation belt region, we find higher wave amplitudes in the LFMrcm, as the compressional waves penetrate deeper, as discussed above. Note that at the smallest radial distances, the wave power in the LFMrcm is a factor of 2 (or more) greater than in the LFMbase simulation. When these differences are considered over the entire azimuthal drift orbit of a radiation belt electron, the effects will lead to different rates of radial transport, as the radial diffusion coefficient is directly proportional to the ULF fluctuations in this frequency range. In summary, it is clear that the plasmaspheric considerations are important for accurate modeling of the radiation belts via MHD test particle simulations.

5. Summary and Conclusions

We have performed a detailed comparison of the plasmaspheric influence on simulated ULF waves in a controlled manner by conducting two simulations (one with a plasmasphere and one without) driven by the same solar wind conditions. In this numerical experiment, we stimulate the magnetospheric ULF waves via broadband ULF fluctuations in the solar wind dynamic pressure. The primary conclusions are as follows:

1. In both simulations, we find that the magnetosphere responds via a quasi-static, forced breathing mode for dynamic pressure fluctuations with periods longer than the Alfvén wave travel time across the dayside magnetosphere (∼4 min).
2. For upstream fluctuations with periods shorter than the dayside Alfvén wave travel time, we find that the magnetosphere responds as a resonant waveguide (in both simulations). Compressional mode energy that enters on the dayside is lost through tailward propagation into the nightside. The compressional wave mode structure near noon MLT is consistent with a radial standing wave oscillation pattern.
3. Our results show that higher-frequency compressional (azimuthal) electric field oscillations penetrate deeper than lower frequency oscillations, due to the frequency dependence in the turning point locations.
4. We find that the inclusion of a plasmasphere has a substantial impact on the physical characteristics of the simulated ULF waves: differences in amplitudes and frequencies, a different number of FLR harmonics, strong broadband wave power at the plasmapause, etc. In addition, the compressional magnetic field oscillations are more robust (larger amplitude, clearer radial eigenmode structure, etc.) in the simulation where the plasmasphere is included. The inclusion of a plasmasphere also leads to a deeper (more earthward) penetration of the compressional (azimuthal) electric field oscillations, due to a shift in the location of the wave turning points. Consequently, the locations where the compressional electric field oscillations couple their energy into local toroidal mode field line resonances also shift earthward.
5. Our analysis suggests that MHD test particle modeling of the radiation belts may misrepresent the particle dynamics if a plasmasphere is not included in the MHD portion of the modeling technique. This is due to the influence that the plasmasphere has on the ULF wave frequency spectrum, spatial distribution, and wave amplitude.

The incorporation of a plasmasphere into the LFM model thus represents an advance in the state of the art in regard to ULF wave modeling with global MHD simulations. However, we note that the implementation of the plasmasphere in the LFM-RCM simulation presented here is a simple, static specification, based on the *Gallagher et al.* [2000] empirical model. This static representation, while an improvement over the stand-alone LFM, is not fully representative of true magnetospheric dynamics. Future work will seek to improve upon the static plasmaspheric representation in the LFM-RCM, eventually leading to a fully dynamic plasmasphere in the simulation (i.e., one that evolves under the influence of the convection and corotation electric fields from the LFM).

Acknowledgments
This material is based upon work that was supported by the National Aeronautics and Space Administration New Hampshire Space grant NNG05GG76H, NASA grants NNX08AM34G and NNX08AI36G, and by the Center for Integrated Space Weather Modeling, which was funded by the Science and Technology Centers program of the National Science Foundation under agreement ATM-0120950. This work was also supported by RBSP-ECT funding provided by JHU/APL contract 967399 under NASA's prime contract NAS5-01072. Work at JHU/APL was supported by NASA grant NNX10AK93G. The National Center for Atmospheric Research is sponsored by the National Science Foundation. All of the simulation data from the present study can be made available upon request to the lead author. One author (S.G.C.) would like to thank Peter Schmitt, Ryan Smith, and Bin Zheng for making available useful analysis routines and to Richard Denton, Mary Hudson, Bill Lotko, John Lyon, and Paul O'Brien for thoughtful discussions. F.R.T. would like to acknowledge Dick Wolf and Stan Sazykin for their many useful contributions in the development of the coupled LFM-RCM code and the support of NASA grant LWS TR & TNNX13AF92G.

References

Allan, W., S. P. White, and E. M. Poulter (1986a), Impulse-excited hydromagnetic cavity and field-line resonances in the magnetosphere, *Planet. Space Sci.*, *34*, 371–385, doi:10.1016/0032-0633(86)90144-3.

Allan, W., E. M. Poulter, and S. P. White (1986b), Hydromagnetic wave coupling in the magnetosphere—Plasmapause effects on impulse-excited resonances, *Planet. Space Sci.*, *34*, 1189–1200, doi:10.1016/0032-0633(86)90056-5.

Baker, D. N., T. I. Pulkkinen, X. Li, S. G. Kanekal, J. B. Blake, R. S. Slesnick, M. G. Henderson, G. D. Reeves, H. E. Spence, and G. Rostoker (1998), Coronal mass ejections, magnetic clouds, and relativistic magnetospheric electron events: ISTP, *J. Geophys. Res.*, *103*, 17,279–17,291.

Boris, J. (1970), A physiclly motivated solution of the Alfvén problem., NRL Memorandum Report, 2167, Washington, D. C.

Chen, L., and A. Hasegawa (1974a), A theory of long-period magnetic pulsations: 1. Steady state excitation of field line resonance, *J. Geophys. Res.*, *79*, 1024–1032, doi:10.1029/JA079i007p01024.

Chen, L., and A. Hasegawa (1974b), A theory of long-period magnetic pulsations: 2. Impulse excitation of surface eigenmode, *J. Geophys. Res.*, *79*, 1033–1037, doi:10.1029/JA079i007p01033.

Claudepierre, S. G., S. R. Elkington, and M. Wiltberger (2008), Solar wind driving of magnetospheric ULF waves: Pulsations driven by velocity shear at the magnetopause, *J. Geophys. Res.*, *113*, A05218, doi:10.1029/2007JA012890.

Claudepierre, S. G., M. Wiltberger, S. R. Elkington, W. Lotko, and M. K. Hudson (2009), Magnetospheric cavity modes driven by solar wind dynamic pressure fluctuations, *Geophys. Res. Lett.*, *36*, L13101, doi:10.1029/2009GL039045.

Claudepierre, S. G., M. K. Hudson, W. Lotko, J. G. Lyon, and R. E. Denton (2010), Solar wind driving of magnetospheric ULF waves: Field line resonances driven by dynamic pressure fluctuations, *J. Geophys. Res.*, *115*, A11202, doi:10.1029/2010JA015399.

Degeling, A. W., R. Rankin, K. Kabin, I. J. Rae, and F. R. Fenrich (2010), Modeling ULF waves in a compressed dipole magnetic field, *J. Geophys. Res.*, *115*, A10212, doi:10.1029/2010JA015410.

Elkington, S. R., M. K. Hudson, and A. A. Chan (2003), Resonant acceleration and diffusion of outer zone electrons in an asymmetric geomagnetic field, *J. Geophys. Res.*, *108*(A3), 1116, doi:10.1029/2001JA009202.

Gallagher, D. L., P. D. Craven, and R. H. Comfort (2000), Global core plasma model, *J. Geophys. Res.*, *105*, 18,819–18,834, doi:10.1029/1999JA000241.

Gombosi, T. I., D. L. de Zeeuw, K. G. Powell, A. J. Ridley, I. V. Sokolov, Q. F. Stout, and G. Toth (2003), Adaptive mesh refinement for global magnetohydrodynamic simulation, in *Space Plasma Simulation, Lecture Notes in Physics*, vol. 615, edited by J. Büchner, C. Dum, and M. Scholer, pp. 247–274, Springer, Berlin.

Green, J. C., and M. G. Kivelson (2001), A tale of two theories: How the adiabatic response and ULF waves affect relativistic electrons, *J. Geophys. Res.*, *106*, 25,777–25,791.

Han, D. S., H. G. Yang, Z. T. Chen, T. Araki, M. W. Dunlop, M. Nose, T. Iyemori, Q. Li, Y. F. Gao, and K. Yumoto (2007), Coupling of perturbations in the solar wind density to global Pi3 pulsations: A case study, *J. Geophys. Res.*, *112*, A05217, doi:10.1029/2006JA011675.

Harel, M., R. A. Wolf, P. H. Reiff, R. W. Spiro, W. J. Burke, F. J. Rich, and M. Smiddy (1981), Quantitative simulation of a magnetospheric substorm: I. Model logic and overview, *J. Geophys. Res.*, *86*, 2217–2241, doi:10.1029/JA086iA04p02217.

Hudson, M. K., S. R. Elkington, J. G. Lyon, and C. C. Goodrich (2000), Increase in relativistic electron flux in the inner magnetosphere: ULF wave mode structure, *Adv. Space Res.*, *25*(12), 2327–2337.

Hudson, M. K., D. N. Baker, J. Goldstein, B. T. Kress, J. Paral, F. R. Toffoletto, and M. Wiltberger (2014), Simulated magnetopause losses and Van Allen Probe flux dropouts, *Geophys. Res. Lett.*, *41*, 1113–1118, doi:10.1002/2014GL059222.

Hughes, W. J. (1994), Magnetospheric ULF waves: A tutorial with a historical prespective, in *Solar Wind Sources of Magnetospheric Ultra-Low-Frequency Waves, Geophysical Monographs*, vol. 81, edited by M. Engebretson, K. Takahashi, and M. Scholer, pp. 1–11, AGU, Washington, D. C.

Kepko, L., and H. E. Spence (2003), Observations of discrete, global magnetospheric oscillations directly driven by solar wind density variations, *J. Geophys. Res.*, *108*(A6), 1257, doi:10.1029/2002JA009676.

Kouznetsov, I., and W. Lotko (1995), Radial energy transport by magnetospheric ULF waves: Effects of magnetic curvature and plasma pressure, *J. Geophys. Res.*, *100*, 7599–7612, doi:10.1029/94JA02293.

Kress, B. T., M. K. Hudson, M. D. Looper, J. Albert, J. G. Lyon, and C. C. Goodrich (2007), Global MHD test particle simulations of >10 MeV radiation belt electrons during storm sudden commencement, *J. Geophys. Res.*, *112*, A09215, doi:10.1029/2006JA012218.

Lee, D., and R. L. Lysak (1999), MHD waves in a three-dimensional dipolar magnetic field: A search for Pi2 pulsations, *J. Geophys. Res.*, *104*, 28,691–28,700, doi:10.1029/1999JA900377.

Lee, D.-H., and R. L. Lysak (1989), Magnetospheric ULF wave coupling in the dipole model—The impulsive excitation, *J. Geophys. Res.*, *94*, 17,097–17,103.

Lee, D.-H., and R. L. Lysak (1991), Impulsive excitation of ULF waves in the three-dimensional dipole model—The initial results, *J. Geophys. Res.*, *96*, 3479–3486, doi:10.1029/90JA02349.

Li, X., I. Roth, M. Temerin, J. R. Wygant, M. K. Hudson, and J. B. Blake (1993), Simulation of the prompt energization and transport of radiation belt particles during the March 24, 1991 SSC, *Geophys. Res. Lett.*, *20*, 2423–2426.

Lyon, J. G., J. A. Fedder, and C. M. Mobarry (2004), The Lyon–Fedder–Mobarry (LFM) global MHD magnetospheric simulation code, *J. Atmos. Solar-Terr. Phys.*, *66*(15), 1333–1350, doi:10.1016/j.jastp.2004.03.020.

Mathie, R. A., and I. R. Mann (2000), A correlation between extended intervals of ULF wave power and storm-time geosynchronous relativistic electron flux enhancements, *Geophys. Res. Lett.*, *27*(20), 3261–3264.

Mathie, R. A., and I. R. Mann (2001), On the solar wind control of Pc5 ULF pulsation power at mid-latitudes: Implications for MeV electron acceleration in the outer radiation belt, *J. Geophys. Res.*, *106*(A12), 29,783–29,796.

Merkin, V. G., and J. G. Lyon (2010), Effects of the low-latitude ionospheric boundary condition on the global magnetosphere, *J. Geophys. Res.*, *115*, A10202, doi:10.1029/2010JA015461.

Northrop, T. G. (1963), *The Adiabatic Motion of Charged Particles*, 109 pp., Interscience Publ., New York.

Ozeke, L. G., I. R. Mann, D. L. Turner, K. R. Murphy, A. W. Degeling, I. J. Rae, and D. K. Milling (2014), Modeling cross L-shell impacts of magnetopause shadowing and ULF wave radial diffusion in the Van Allen Belts, *Geophys. Res. Lett.*, *41*(19), 6556–6562, doi:10.1002/2014GL060787.

Paulikas, G. A., and J. B. Blake (1979), Effects of the solar wind on magnetospheric dynamics: Energetic electrons at the synchronous orbit, in *Quantitative Modeling of Magnetospheric Processes*, edited by W. P. Olson, pp. 180–202, AGU, Washington, D. C.

Pembroke, A., F. Toffoletto, S. Sazykin, M. Wiltberger, J. Lyon, V. Merkin, and P. Schmitt (2012), Initial results from a dynamic coupled magnetosphere-ionosphere-ring current model, *J. Geophys. Res.*, *117*, A02211, doi:10.1029/2011JA016979.

Percival, D. B., and A. T. Walden (1993), *Spectral Analysis for Physical Applications*, 580 pp., Cambridge Univ.

Proehl, J. A., W. Lotko, I. Kouznetsov, and S. D. Geimer (2002), Ultralow-frequency magnetohydrodynamics in boundary-constrained geomagnetic flux coordinates, *J. Geophys. Res.*, *107*, 1225, doi:10.1029/2001JA000135.

Raeder, J., Y. Wang, and T. J. Fuller-Rowell (2001), Geomagnetic storm simulation with a coupled magnetosphere- ionosphere-thermosphere model, in *Space Weather, Geophys. Monogr. Ser.*, vol. 125, edited by J. Raeder, Y. Wang, and T. J. Fuller-Rowell, pp. 377–384, AGU, Washington, D. C.

Reeves, G. D., et al. (2013), Electron acceleration in the Heart of the Van Allen radiation belts, *Science*, *341*, 991–994, doi:10.1126/science.1237743.

Richmond, A. D. (1992), Assimilative mapping of ionospheric electrodynamics, *Adv. Space Res.*, *12*, 59–68, doi:10.1016/0273-1177(92)90040-5.

Rickard, G. J., and A. N. Wright (1994), Alfven resonance excitation and fast wave propagation in magnetospheric waveguides, *J. Geophys. Res.*, *99*, 13,455–13,464, doi:10.1029/94JA00674.

Rostoker, G., S. Skone, and D. N. Baker (1998), On the origin of relativistic electrons in the magnetosphere associated with some geomagnetic storms, *Geophys. Res. Lett.*, *25*, 3701–3704.

Samson, J. C., B. G. Harrold, J. M. Ruohoniemi, R. A. Greenwald, and A. D. M. Walker (1992), Field line resonances associated with MHD waveguides in the magnetosphere, *Geophys. Res. Lett.*, *19*, 441–444.

Sazykin, S. (2000), Theoretical studies of penetration of magnetospheric electric fields to the ionosphere, PhD thesis, Utah State Univ.

Schulz, M., and L. J. Lanzerotti (1974), *Particle Diffusion in the Radiation Belts, Physics and Chemistry in Space*, 215 pp., vol. 7, Springer, New York.

Shprits, Y. Y., R. M. Thorne, R. Friedel, G. D. Reeves, J. Fennell, D. N. Baker, and S. G. Kanekal (2006), Outward radial diffusion driven by losses at magnetopause, *J. Geophys. Res.*, *111*, A11214, doi:10.1029/2006JA011657.

Takahashi, K., and A. Y. Ukhorskiy (2007), Solar wind control of Pc5 pulsation power at geosynchronous orbit, *J. Geophys. Res.*, *112*, A11205, doi:10.1029/2007JA012483.

Takahashi, K., J. Bonnell, K.-H. Glassmeier, V. Angelopoulos, H. J. Singer, P. J. Chi, R. E. Denton, Y. Nishimura, D.-H. Lee, M. Nosé, and W. Liu (2010), Multipoint observation of fast mode waves trapped in the dayside plasmasphere, *J. Geophys. Res.*, *115*, A12247, doi:10.1029/2010JA015956.

Tan, L. C., X. Shao, A. S. Sharma, and S. F. Fung (2011), Relativistic electron acceleration by compressional-mode ULF waves: Evidence from correlated cluster, Los Alamos National Laboratory spacecraft, and ground-based magnetometer measurements, *J. Geophys. Res.*, *116*, A07226, doi:10.1029/2010JA016226.

Thomson, D. J. (1982), Spectrum estimation and harmonic analysis, *Proc. IEEE*, *70*, 1055–1096.

Thorne, R. M. (2010), Radiation belt dynamics: The importance of wave-particle interactions, *Geophys. Res. Lett.*, *37*, L22107, doi:10.1029/2010GL044990.

Thorne, R. M., et al. (2013), Rapid local acceleration of relativistic radiation-belt electrons by magnetospheric chorus, *Nature*, *504*, 411–414, doi:10.1038/nature12889.

Toffoletto, F., S. Sazykin, R. Spiro, and R. Wolf (2003), Inner magnetospheric modeling with the Rice Convection Model, *Space Sci. Rev.*, *107*, 175–196, doi:10.1023/A:1025532008047.

Waters, C. L., and M. D. Sciffer (2008), Field line resonant frequencies and ionospheric conductance: Results from a 2-D MHD model, *J. Geophys. Res.*, *113*, A05219, doi:10.1029/2007JA012822.

Waters, C. L., B. G. Harrold, F. W. Menk, J. C. Samson, and B. J. Fraser (2000), Field line resonances and waveguide modes at low latitudes. 2. A model, *J. Geophys. Res.*, *105*, 7763–7774, doi:10.1029/1999JA900267.

Wiltberger, M., R. S. Weigel, W. Lotko, and J. A. Fedder (2009), Modeling seasonal variations of auroral particle precipitation in a global-scale magnetosphere-ionosphere simulation, *J. Geophys. Res.*, *114*, A01204, doi:10.1029/2008JA013108.

Wolf, R. A., R. W. Spiro, and F. J. Rich (1991), Extension of convection modeling into the high-latitude ionosphere—Some theoretical difficulties, *J. Atmos. Sol. Terr. Phys.*, *53*, 817–829.

Wright, A. N. (1994), Dispersion and wave coupling in inhomogeneous MHD waveguides, *J. Geophys. Res.*, *99*, 159–167, doi:10.1029/93JA02206.

Wright, A. N., W. Allan, R. D. Elphinstone, and L. L. Cogger (1999), Phase mixing and phase motion of Alfvén waves on tail-like and dipole-like magnetic field lines, *J. Geophys. Res.*, *104*, 10,159–10,176, doi:10.1029/1999JA900018.

Zong, Q.-G., X.-Z. Zhou, Y. F. Wang, X. Li, P. Song, D. N. Baker, T. A. Fritz, P. W. Daly, M. Dunlop, and A. Pedersen (2009), Energetic electron response to ULF waves induced by interplanetary shocks in the outer radiation belt, *J. Geophys. Res.*, *114*, A10204, doi:10.1029/2009JA014393.